esa climate change initiative

European Space Agency

# Product User Guide (PUG)

glaciers cci

| | |
|---|---|
| Prepared by: | Glaciers_cci consortium |
| Contract: | 4000127593/19/I-NB |
| Name: | Glaciers_cci+D4.1_PVIR |
| Version: | 1.0 |
| Date: | 04.04. 2022 |


Contact:
Frank Paul
Department of Geography
University of Zurich
frank.paul@geo.uzh.ch

Technical Officer:
Anna Maria Trofaier
ESA Climate Office


UNIVERSITY OF OSLO

University of Zurich[UZH]

UNIVERSITY OF LEEDS

GAMMA REMOTE SENSING

enveo

# Document status sheet

| Version | Date | Changes | Approval |
|---|---|---|---|
| 0.1 | 15.02. 2022 | Initial draft | |
| 1.0 | 04.04. 2022 | Consortium input integrated | |

The work described in this report was done under ESA contract 4000127593/19/I-NB. Responsibility for the contents resides with the authors who prepared it.

Author team:
Tazio Strozzi, Andreas Wiesmann (Gamma), Jan Wuite, Thomas Nagler, Ludivine Libert (ENVEO), Frank Paul, Philipp Rastner (GIUZ), Andreas Kääb, Désirée Treichler, Livia Piermattei (GUIO), Lin Gilbert, Andrew Shepherd (SEEL)

Glaciers_cci Technical Officer at ESA:
Anna Maria Trofaier

# Table of Contents

# 1. Introduction

## 1.1 Purpose and Scope

This document is the Product User Guide (PUG) for the Glaciers CCI+ project. It refers to the datasets generated for the two use cases in the Eastern Arctic and High Mountain Asia (HMA) that can be downloaded from cryoportal.enveo.at. For each of the four products generated (outlines, elevation changes from altimetry and DEM differencing, flow velocity) we describe product content and format as well as known limitations and software tools to view the datasets, split for the two use cases, if applicable. Table 1.1 in the next section is providing a condensed overview on the datasets provided. For each of the four products, reference to [RD1] is made, if applicable, so that in this document only innovative aspects are described.

## 1.2 Dataset overview

*Table 1.1: Overview of the datasets described in this PUG. The entries for the use case Eastern Arctic are shaded in grey. ECA: Elevation change from Altimetry, IV: Ice velocity.*

| Product | Description | Epoch | Format | Size | Count |
|---|---|---|---|---|---|
| Area | Multitemporal extents for 3 glaciers | 1973-2021 | shp | 100 kB | 1 file |
| ECA | Elevation profiles ICESat-2 - DEM | 2000-2021 | csv | 44 MB | 1 file |
| DEM | HMA DEM - SRTM | 2000-2015 | geotiff | 1.4 MB | 1 file |
| IV | Landsat 7 ETM+, Landsat 8 OLI | 09.00-07.19 | geotiff | 5.3 MB | 7 files |
| IV | Sentinel-2A | 11.16-10.20 | geotiff | 4.5 MB | 7 files |
| IV | Sentinel-2A | 09.19-05.21 | geotiff | 14.3 MB | 19 files |
| IV | PlanetScope | 06.20-10.20 | geotiff | 4.5 MB | 13 files |
| IV | Chongtar-Baltoro region in the Karakoram from TerraSAR-X offset tracking | 2011-2014 | geotiff | 20 MB | 3 files |
| Area | Glacier outlines Franz-Josef-Land: | | | | 1 file |
| | Corona | 1962 | shp | 4 MB | |
| | Sentinel-2 | 2016 | shp | 7 MB | |
| Area | Inventory of glacier surges over Svalbard | 2017-2021 | csv | 1.4 KB | 1 file |
| ECA | Surface modelling and time series, Svalbard: | | | | |
| | ERS1 | 08.91-05.96 | netCDF | 317 MB | 1 file |
| | ERS2 | 05.95-07.03 | netCDF | 528 MB | 1 file |
| | EnviSat | 09.02-04.12 | netCDF | 610 MB | 1 file |
| | CryoSat-2 | 10.10-11.20 | netCDF | 646 MB | 1 file |
| | Sentinel-3A | 12.16-12.20 | netCDF | 265 MB | 1 file |
| | Sentinel-3B | 12.18-12.20 | netCDF | 136 MB | 1 file |
| ECA | Surface modelling & time series, Franz-Josef- Land: | | | | |
| | ERS1 | 08.91-05.96 | netCDF | 185 MB | 1 file |
| | ERS2 | 05.95-07.03 | netCDF | 308 MB | 1 file |
| | EnviSat | 09.02-04.12 | netCDF | 356 MB | 1 file |
| | CryoSat-2 | 10.10-11.20 | netCDF | 383 MB | 1 file |
| | Sentinel-3A | 12.16-12.20 | netCDF | 164 MB | 1 file |
| | Sentinel-3B | 12.18-12.20 | netCDF | 89 MB | 1 file |
| ECA | Surface modelling and time-series, Novaya Zemlya: | | | | |
| | ERS1 | 08.91-05.96 | netCDF | 381 MB | 1 file |
| | ERS2 | 05.95-07.03 | netCDF | 635 MB | 1 file |

| | | | | | |
|---|---|---|---|---|---|
| | EnviSat | 09.02-04.12 | netCDF | 734 MB | 1 file |
| | CryoSat-2 | 10.10-11.20 | netCDF | 790 MB | 1 file |
| | Sentinel-3A | 12.16-12.20 | netCDF | 332 MB | 1 file |
| | Sentinel-3B | 12.18-12.20 | netCDF | 183 MB | 1 file |
| ECA | Surface modelling and time-series, Severnaya Zemlya: | | | | |
| | ERS1 | 08.91-05.96 | netCDF | 132 MB | 1 file |
| | ERS2 | 05.95-07.03 | netCDF | 220 MB | 1 file |
| | EnviSat | 09.02-04.12 | netCDF | 255 MB | 1 file |
| | CryoSat-2 | 10.10-11.20 | netCDF | 274 MB | 1 file |
| | Sentinel-3A | 12.16-12.20 | netCDF | 115 MB | 1 file |
| | Sentinel-3B | 12.18-12.20 | netCDF | 61 MB | 1 file |
| IV | Eastern Arctic from Offset-Tracking of Past Spaceborne Satellite SAR data: | | | | |
| | JERS-1 Svalbard | 1993-1998 | vector | 911 MB | 1 file |
| | JERS-1 Franz-Josef-Land | 1996-1998 | vector | 2.4 GB | 1 file |
| | JERS-1 Novaya Zemlya | 1998 | vector | 600 MB | 1 file |
| | ERS-1 Svalbard | 1992 | vector | 235 MB | 1 file |
| | ERS-1 Franz-Josef-Land | 1991 | vector | 133 MB | 1 file |
| | ERS-1 Severnaya Zemlya | 1991-1992 | vector | 359 MB | 1 file |
| | ALOS-1 PALSAR-1 Svalbard | 2007-2011 | vector | 340 MB | 1 file |
| | ALOS-1 PALSAR-1 Franz-Josef-Land | 2010-2011 | vector | 213 MB | 1 file |
| | ALOS-1 PALSAR-1 Novaya Zemlya | 2008-2010 | vector | 751 MB | 1 file |
| IV | Svalbard from ERS-1/2 InSAR | 1995-1997 | geotiff | 684 MB | 2 files |
| IV (*) | Eastern Arctic from Offset-Tracking of Sentinel-1 SAR data: | | | | |
| | Svalbard | 2015-2022 | vector | 143 GB | 704 files |
| | Franz-Josef-Land | 2015-2021 | vector | 28 GB | 99 files |
| | Novaya Zemlya | 2015-2021 | vector | 48 GB | 245 files |
| | Severnaya Zemlya | 2015-2021 | vector | 35 GB | 328 files |
| IV | Eastern Arctic from Offset-Tracking of Sentinel-1 SAR data: | | | | |
| | Svalbard | 01-02.2021 | geotiff | 141 MB | 1 file |
| | Franz-Josef-Land | 01-02.2021 | geotiff | 62 MB | 1 file |
| | Novaya Zemlya | 02.2021 | geotiff | 118 MB | 1 file |
| | Severnaya Zemlya | 01-02.2021 | geotiff | 84 MB | 1 file |
| IV | Svalbard from Sentinel-1 InSAR | 2018-2019 | geotiff | 270 MB | 1 file |
| IV | Svalbard from Sentinel-1 InSAR & Offset-Tracking | 2018-2019 | geotiff | 250 MB | 1 file |

## 1.3 Related Documents

| Acronym | Title | Document reference | Version | Date |
|---|---|---|---|---|
| [RD1] | Product User Guide | Glaciers_cci-D3.3_PUG | 1.6 | 05.10.2017 |
| [RD2] | Product Validation Plan | Glaciers_cci+D1.3-2_PVP | 2.1 | 10.10.2021 |
| [RD3] | Climate Research Data Package | Glaciers_cci+D3.2_CRDPv2 | 1.0 | 08.10.2021 |
| [RD4] | Algorithm Theoretical Basis Document | Glaciers_cci+D2.1_ATBD | 0.3 | 19.06.2020 |
| [RD5] | Product Validation and Intercomparison Report | Glaciers_cci+D4.1_PVIR | 1.0 | 10.11.2021 |
| [RD6] | User Requirements Document | Glaciers_cci+D1.1-2_URD | 2.1 | 17.11.2021 |

# 2. Glacier extent

## 2.1 Product content

### 2.1.1 Multi-temporal glacier extents Karakoram

For our study about the three glacier surges in the Karakoram (Paul et al. in rev.), we created multi-temporal outlines by manual digitising of glacier extents on time-series of mostly Landsat satellite images (Fig. 2.1). As a starting point, the GAMDAM II glacier inventory by Sakai (2019) was used. It was first slightly edited (removing seasonal snow, disconnecting tributaries) before theoretical maximum glacier extents were digitized for each of the three glaciers. These were later also used to constrain the region for all glacier-specific calculations (elevation changes and velocities) and to define regions off glaciers (e.g. for uncertainty assessment over stable ground). As the termini of all three glaciers could end on top of the main glacier (Sarpo Laggo) in the valley floor, it was decided to cut its extent back to the distinct tear-drop shaped moraine from Moni Glacier (Fig. 2.1). The three individual glacier polygons for each glacier were then cut into multiple sections by digitizing a polygon split line along the terminus position of the respective year. The timing of the related satellite scenes was chosen to have at least a two-pixel difference between the lines. The digitized extents cover the surge phase of South Chongtar Glacier in 2020/21, of North Chongtar from 1973 on (starting with Landsat MSS scenes) and of a glacier named NN9 from 2000 to 2021. Each image date was manually entered in the attribute table for each extent and later used for the colour-coded visualization of extents shown in Fig. 2.1. The multi-temporal outlines within the outer outline are only used for the purpose of this visualization.

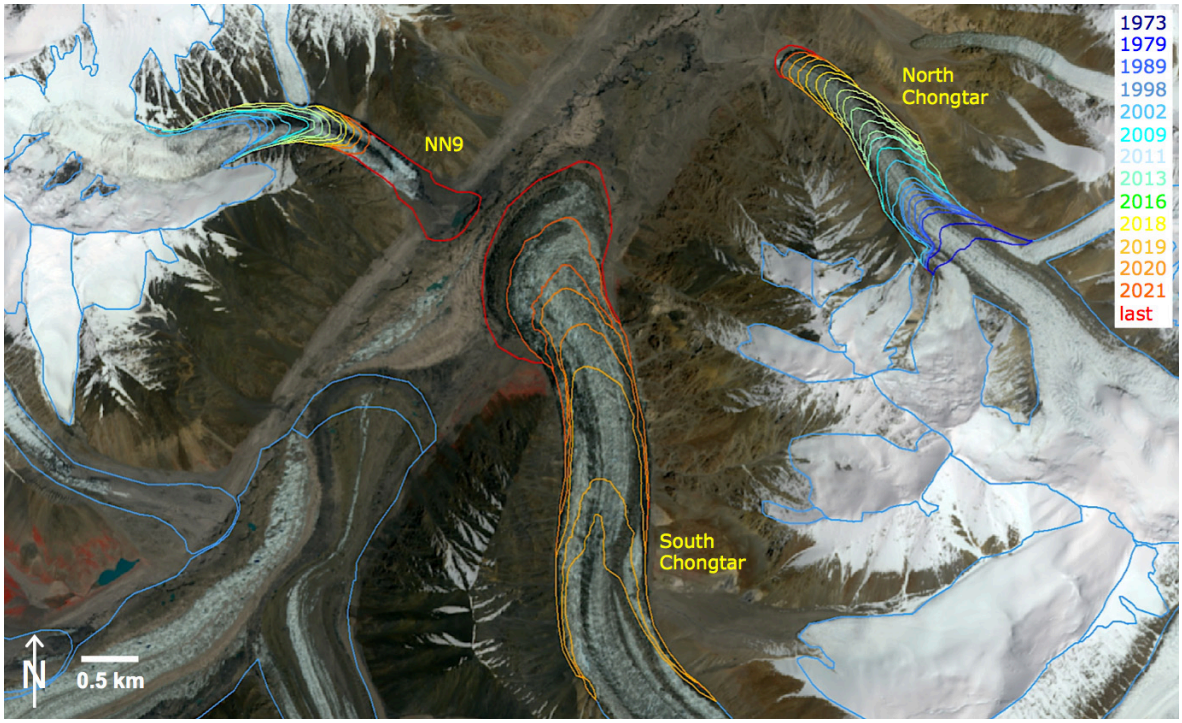


*Figure 2.1: Colour-coded visualization of multi-temporal glacier extents as used for a figure in the study by Paul et al. (in rev.).*

### 2.1.2 Glacier extents Franz Josef Land 1962 and 2016

This product is actually containing two products, glacier outlines for 1962 as derived from manual digitizing of orthorectified Corona scenes and a full glacier inventory for 2016 as derived from Sentinel-2 scenes and the ArcticDEM (Fig. 2.2). More general information about product content (e.g. glacier definitions and interpretation of specific features) can be found in Section 2.1 of the PUG of Glaciers_cci [RD1]. We here only mention that most of the Sentinel-2 scenes used for the mapping have been acquired under near-optimal mapping conditions in Sep 2016 (without seasonal snow off and partly also on glaciers), whereas the image stripes from Corona KH4 have all been acquired at the same day (18.9.1962) but all glaciers (and parts of the terrain) are covered under a thin layer of snow.

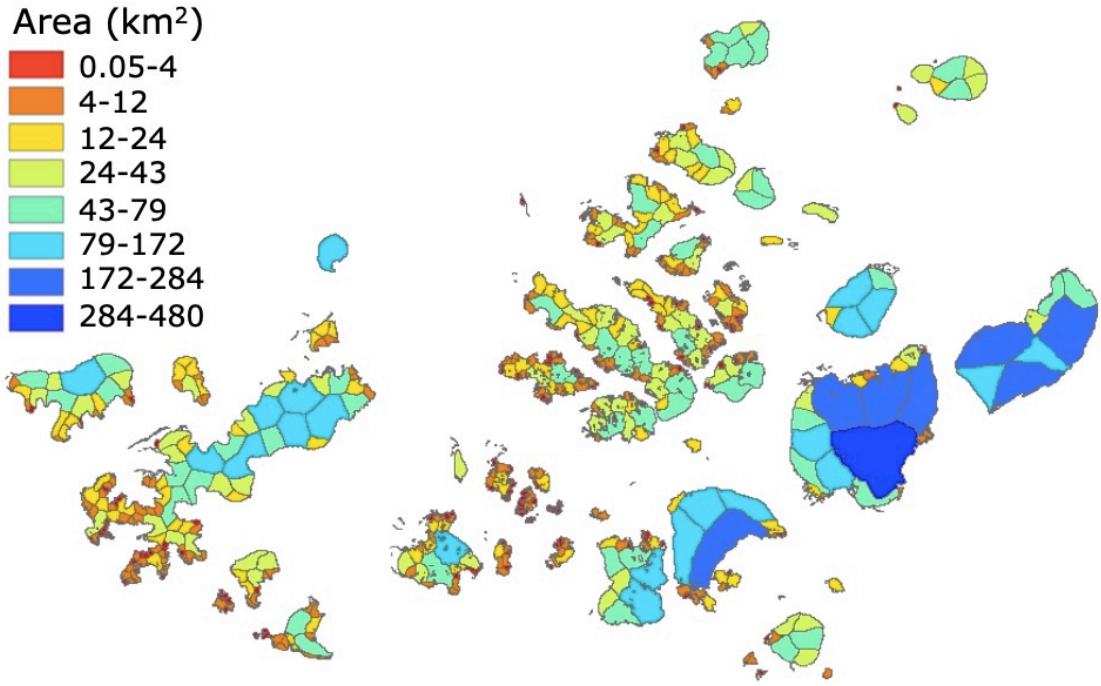


*Figure 2.2: Colour-coded glacier area from the 2016 inventory of Franz-Josef-Land.*

The outlines were derived automatically from Sentinel-2 with local manual corrections for glaciers in shadow or under debris cover or clouds (see Section 2.1 in ATBD, [RD4]) and by manual delineation of extents as visible in the orthorectified Corona KH-4 mosaic (see Section 2.4 in [RD4] for details of the processing). Ice divides were derived automatically from the ArcticDEM using a watershed algorithm and then manually corrected and selected following the glacier separation in RGI6. Topographic information for each glacier was calculated from the ArcticDEM and tidewater glaciers were manually selected and marked. Further details will be provided in a publication that is in preparation.

### 2.1.3 Surge inventory over Svalbard 2017-2022

The inventory of surging glaciers over Svalbard (Fig. 2.3) is based on annual Sentinel-1 backscatter differences, winter to winter, where significantly increasing backscatter is interpreted as increased crevassing due to starting surge-type activity [RD4]. Vice-versa, strongly decreasing backscatter activity is interpreted as a decreasing or ending surge. Validation with Sentinel-1 derived glacier velocity changes indicates a high robustness of the product. The product is meant to be included into the RGI global glacier inventory.


*Figure 2.3: Surge-type activity 2017-2022 over Svalbard observed from Sentinel-1 backscatter changes.*

## 2.2 Product format

### 2.2.1 Multi-temporal glacier extents Karakoram

The dataset is provided in shape file format with polyline topology. The attribute table contains items from the GAMDAM II inventory (e.g. IDs, Landsat path / row and date) as well as the new attributes date (dd.mm.yyyy) and year, decoding the day within a year by a decimal after the year (e.g. 1 July 2020 would be 2020.5). This allows a colour-coded visualization of the outlines as shown in Fig. 2.1.

### 2.2.2 Glacier extents Franz Josef Land 1962 and 2016

The outlines from 1962 are provided in shape file format and contain the attributes ID, area and tide_water. The area is given in $km^2$ and tide_water has an entry '1' if the glacier is a tide-water glacier (i.e. its terminus is in contact with the ocean) or zero otherwise. Topographic information has not been derived for the individual glaciers, as an accurate DEM for this point in time was not available. Also the outlines from 2016 are provided in shape file format, but contain the full suite of information required for a glacier inventory (see Table 2.1). A metadata information sheet contains further details about the data processing and satellite scenes used and is available from the Glaciers_cci database (http://glaciers-cci.enveo.at). The raw satellite data used to map glacier extents are provided freely e.g. from earthexplorer.usgs.gov in the jp2 (jpeg 2000) format for Sentinel-2 and as a tif file in the case of Corona KH-4. For further data processing the already orthorectified (L1C) images from Sentinel-2 are converted to geotif format. The Corona stripes were orthorectified with the ArcticDEM, mosaicked and exported to a geotif file at 10 m spatial resolution. As stated above, this mosaic was also used for the (mostly manual) digitizing of glacier extents.

*Table 2.1: Attribute information for the 2016 glacier inventory.*

| Attribute | Format | Content |
|---|---|---|
| Glacier_nr | Integer | Identifier |
| LAT | Float | Longitude of glacier centroid (deg) |
| LON | Float | Latitude of glacier centroid (deg) |
| Area_km2 | Float | Area of glacier ($km^2$) |
| Elev_min | Float | Minimum elevation (m) |
| Elev_max | Float | Maximum elevation (m) |
| Elev_mean | Float | Mean elevation (m) |
| Elev_med | Integer | Median elevation (m) |
| Slope_mean | Float | Mean surface slope (°) |
| Asp_mean | Float | Mean aspect (°) |
| Sec_nr | Integer | Number of the aspect sector (1: N, 2: NE, ...) |
| Sec_name | Character | Name of the aspect sector (N, NE, E, SE, ...) |
| Marine_ter | Integer | Marine terminating (Yes=1, No=0) |
| Date | YYYY-MM-DD | Date of satellite image used |
| Funding | Character | Funding sources (project names) |
| Analyst | Character | Names of the analysts |
| Scene_ID | Character | Sensor_Tile_Date (S2-40XEQ_20160912) |
| O1_region | Character | First order region |
| O2_region | Character | Second order region |
| Name_isl | Character | Name of the island |
| Island_ID | Integer | Numeric code for the island |

### 2.2.3 Surge inventory over Svalbard 2017-2022

Procuct format is a csv text file, with columns GLIMS-ID, RGI-ID, approx. longitude, approx. latitude, RGI surge type ('3' for 'observed surge'), and a comment field.

## 2.3 Known limitations

### 2.3.1 Multi-temporal glacier extents Karakoram

The dataset was only created to illustrate the largely different surge behaviours of the three glaciers in the publication (Paul et al. in rev.). It has not been used to determine changes of the glacier front. These were measured manually using several further satellite images.

### 2.3.2 Glacier extents Franz Josef Land 1962 and 2016

Most land in the Corona images from 1962 was covered by a thin layer of snow. This resulted in local uncertainties of the glacier mapping, i.e. it could be possible that glacier extents are too large as snow cover has been mapped. This mostly impacts the lower limits of glaciers on land (Fig. 2.4). Other analysts will likely interpret extents of these glaciers differently. It has also to be noted that the spatial co-registration of the Corona scenes is not 100% exact and locally small shifts of the outlines can be seen. They are in general much smaller than the area changes from 1962 to 2016, but some caution with the interpretation is advised. A few glaciers in the September 2016 images were covered by mostly thin and often semi-transparent clouds. To properly delineate also this part, we used additional scenes from July 2016 without clouds but substantial seasonal snow cover. This has no impact for the extents of the tide water glaciers, but the extent of some smaller land-terminating glaciers could have been overestimated. However, in most cases the glacier extent could also be identified under snow cover.

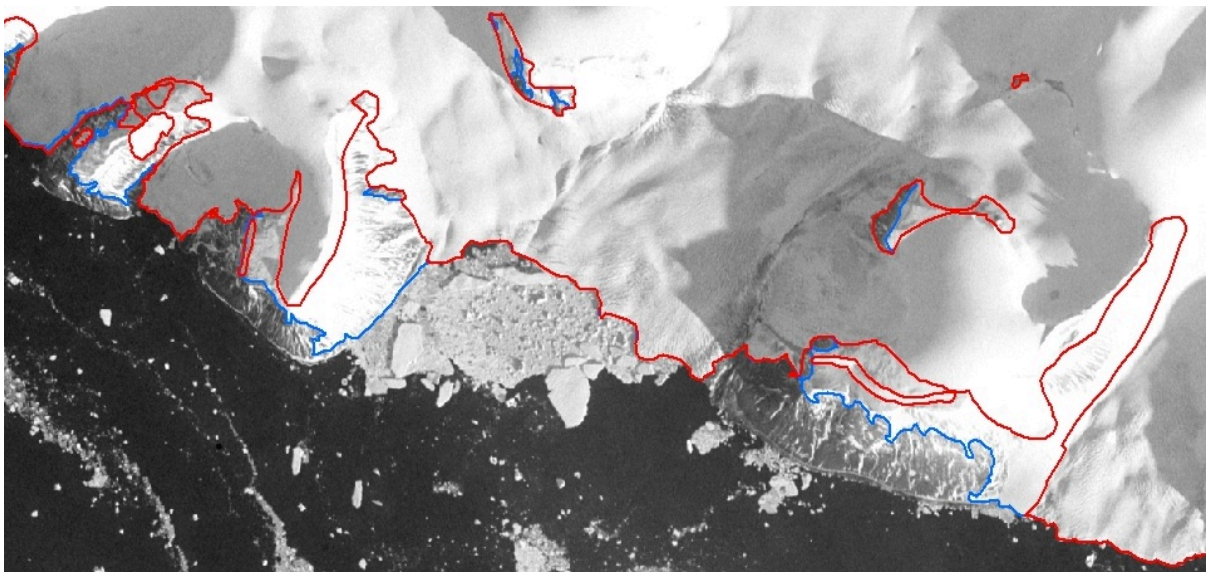

*Figure 2.4: Differences in the interpretation of glacier extents in Franz-Josef-Land for the snow-covered Corona scene between two analysts. The originally larger extents (blue) were corrected back (or in the case of rock outcrops increased) to the red extents by the second analyst.*

### 2.3.3 Surge inventory over Svalbard 2017-2022

The product is based on operator-based visual identification of surges in backscatter-change images. As such, the operator might miss minor surges with little backscatter changes, even if validation of the product points to high robustness and completeness. Not all events marked in the product might qualify as 'surges' in all possible definition of surges. For example, the product is not directly reflecting the magnitude of ice velocities, often defined as being at least one order of magnitude higher than quiescent-phase velocities of the same glacier.

## 2.4 Software tools and data access

### 2.4.1 Multi-temporal glacier extents Karakoram

The shape file format is open and can be viewed with various free and commercial software products. Also the satellite images used to create the outlines are freely available (e.g. from earthexplorer.usgs.gov) and can be viewed with free and commercial software packages.

### 2.4.2 Glacier extents Franz Josef Land 1962 and 2016

Glacier outlines from both datasets are in shape file format that is open and can be viewed with numerous free and commercial software products. Also the satellite images used to create the outlines are freely available (e.g. from earthexplorer.usgs.gov) and can be viewed with several free and commercial software packages.

### 2.4.3 Surge inventory over Svalbard 2017-2022

The product is a simple text file with geographic coordinates that can easily be plotted in GIS systems or Google Earth (Fig. 2.3). It can also be merged with the RGI through its RGI / GLIMS IDs.

# 3. Elevation change (Altimetry)

## 3.1 Product content

### 3.1.1 Elevation change profiles in HMA from ICESat-2 data

Elevation change from satellite altimetry data is estimated either from comparing repeat overpasses of the same sensor type, or by comparing satellite altimetry with a reference DEM in regions where satellite overpasses are not repeated exactly. The latter is the case for ICESat-2 spaceborne laser altimetry for all areas outside the Arctic/Antarctic. Due to the current systematic off-pointing at mid-latitudes, ICESat-2 data tracks available up to now are shifted by several kilometres in space everywhere but in polar regions. The Advanced Topographic Laser Altimeter System (ATLAS) instrument on-board ICESat-2 acquires elevation profiles at a 91-day temporal resolution since October 2018. Each satellite overpass results in three beam pairs that are separated by 3.3 km and 90 m between/within pairs, respectively (Markus et al., 2017). One ICESat-2 overpass yields six parallel elevation profiles. ICESat-2 ATLAS data is distributed in several product versions with varying along-track resolution. The ICESat-2 ATL03 Global Geolocated Photon Data product (Neumann et al., 2021) provides surface elevation measurements from individual photons every 0.7 m along the elevation profiles. Individual measurements correspond to footprints of ca. 11 m in diameter. The ICESat-2 ATL06 and ATL08 datasets are higher-level derivative of the ATL03 product and provide geolocated land ice/land surface surface heights with 40/100 m spatial resolution in profile direction, respectively.

The ATL03 data provides a very good vertical accuracy and along-profile resolution that reveals details of glacier surface topography. The two closest repeating pairs of tracks in the HMA case study area (Chongtar area) are several hundred metres apart, which is too much for a direct comparison given the steep, rugged glacier surfaces in the area. Elevation changes from ICESat-2 altimetry data in this area are thus given with regard to full coverage Digital Elevation Models (DEMs), namely the SRTM1 DEM at 1 arcsec (~30 m) resolution (USGS, 2020) and the HMA-DEM mosaic (Shean, 2017) further described in Section 4 (DEM differencing). Compared to the sparse temporal availability of DEMs, the more frequent ICESat-2 overpasses provide additional temporal information on glacier surface changes in particular for areas with rapid changes, such as the surges in the Chongtar area. The product contains data from 2.5 years (autumn 2018 through spring 2021), which corresponds to 42 intersections with the centrelines of three investigated glaciers: 23 on South Chongtar (from seven dates), 13 on North Chongtar (from six dates), and 6 on NN9 (from three dates).

### 3.1.2 Surface modelling and time-series over the Eastern Arctic

Elevation change estimates for the four Eastern Arctic regions of interest were generated on 1 km x 1 km grids in EPSG 3413 (north polar stereographic projection), for each of six satellite radar altimetry missions. All possible data was retrieved, i.e. from every surface type and every instrumental mode, so that the user may apply their own surface masking if they wish. The grids are summarised in Table 3.1 and the missions in Table 3.2.

In processing, each grid cell was treated separately. First a surface model was fitted to the data, and residual elevation anomalies derived. Then a second model was fitted to remove short-period fluctuations correlated with backscatter power changes. Finally, correction for glacial

isostatic adjustment was applied to each elevation in the resulting time-series, using the ICE-5G model (see Peltier 2004). The surface model was used to estimate the surface elevation change rate during the mission, and also the slope of the surface within the grid cell. For full details see [RD4].

The processing code used is part of the Centre for Polar Observation and Monitoring (CPOM) software system, developed over a period of years for multiple cryosphere projects, see https://cpom.org.uk/operational-polar-monitoring.

*Table 3.1: Elevation change from altimetry product, missions summary.*

| Region | Grid size, x by y | Extreme bottom left grid co-ordinates, x,y [m] |
|---|---|---|
| Svalbard | 400 x 600 | 900, -800 |
| Franz Josef Land | 650 x 500 | 1250, 150 |
| Novaya Zemlya | 350 x 450 | 800, -50 |
| Severnaya Zemlya | 250 x 450 | 550, 650 |

*Table 3.2: Elevation change from altimetry product, regional grid summary.*

| Mission | Data baseline | Data period |
|---|---|---|
| ERS1 | Reaper | August 1991 – May 1996 |
| ERS2 | Reaper | May 1995 – July 2003 |
| EnviSat | GDRv3 | September 2002 – April 2012 |
| CryoSat-2 | Baseline D (the altimeter operated only in SARIn mode in these regions) | October 2010 – November 2020 |
| Sentinel-3A | SR_2_LAN_NT baseline 4 | December 2016 – December 2020 |
| Sentinel-3B | SR_2_LAN_NT baseline 4 | December 2018 – December 2020 |

## 3.2 Product format

### 3.2.1 Elevation change profiles in HMA from ICESat-2 data

The provided dataset contains surface elevation profiles with elevation data from three time stamps. ICESat-2 ATL03 (v4) and DEM data were filtered and re-projected, and for each ATL03 elevation measurement, respectively, the corresponding surface elevations of the SRTM DEM from February 2000 and the HMA DEM mosaic from spring/summer 2015 are provided. The dataset covers the South Chongtar Glacier, NN9/NN08/NN07 glaciers, North Chongtar and Sarpo Laggo glaciers, all located in the central Karakoram at approximately 35.94° N and 76.33° E. The dataset contains columns that identify individual ICESat-2 over-passes (date), tracks (pair_beam) and glaciers (glacier_id, glacier_name). Elevation differences (Fig. 3.1) are obtained by subtracting two elevation data columns of the dataset.

The zip file contains a data file in csv format with acquisition time stamps, coordinates, elevation data, and glacier classification, along with a metadata text file explaining the data column names. All elevations are in metres above the WGS 84 ellipsoid and the projection is WGS 84 / UTM zone 43N as well as geographical coordinates (latitude/longitude).

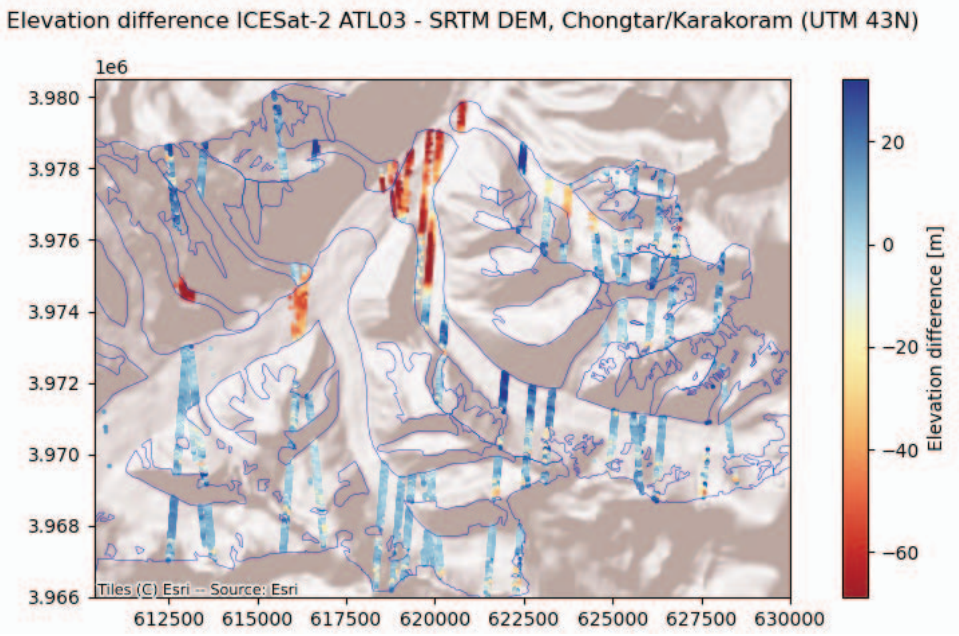


*Figure 3.1: Elevation differences between ICESat-2 data from 2018-2021 and the SRTM DEM from 2000.*

### 3.2.2 Surface modelling and timeseries over the Eastern Arctic

The product consists of a metadata file and a data file for each region and mission. The metadata file is a Word document, and the data file is in netCDF4 format.

***File naming convention***

The convention for a metadata file is;
ec_altimetry_mission_region_surface_fit_metadata.docx
The convention for a data file is;
ec_altimetry_mission_region_surface_fit_and_epoch_average.nc
In each case

- ec indicates that this is an elevation change product
- altimetry indicates the sensor type
- mission is the satellite mission that carried the sensor – allowed missions are
  - e1 = ERS1
  - e2 = ERS2
  - ev = EnviSat
  - cs2 = CryoSat-2
  - s3a = Sentinel-3A
  - s3b = Sentinel-3B
- region is the geographical area covered – allowed regions are
  - svalbard
  - franz_josef_land
  - novaya_zemlya
  - severnaya_zemlya
- surface_fit indicates that the file contains information from a surface fitting algorithm
- epoch_average indicates that the file contains time-series of elevation change

***Metadata***

The metadata for a given mission and region is held in one Word document. The information is given in a format common to all Glaciers_cci+ products, and not all items are relevant to the altimetry product. The information given is listed in Table 3.3. An example of the figure given in the metadata is in Fig. 3.2, where the elevation change rates come from the data file, and the background image and coastline come from the freely available Natural Earth map dataset at https://www.naturalearthdata.com.

*Table 3.3: Elevation change from altimetry product, metadata file format.*

| Item | Description |
|---|---|
| Name | Dataset name, including mission and region |
| Description | Brief description of dataset |
| Source | Source of data used to make dataset |
| Reference | Reference to product handbook (or similar) of data source |
| Temporal coverage | Time range of source data included in dataset |
| Temporal resolution<br>Spatial coverage | Not applicable for surface fitting, as the exact measurement times throughout the mission are used. However, the accompanying epoch-averaged time-series are given at a 30 day resolution. |
| SpatialVertical coverage | The name of the region covered |
| SpatialTemporal resolution | 1 km x 1 km grid |
| Vertical coverage | Not applicable, only the surface is considered |
| Vertical resolution | Not applicable, only the surface is considered |
| Map projection | EPSG reference of map projection – always EPSG 3413 |
| File format | Format of data file – always netCDF4 |
| Figure | Plot of surface elevation change rate derived from the surface fitting algorithm over the whole mission period, on regional grid |

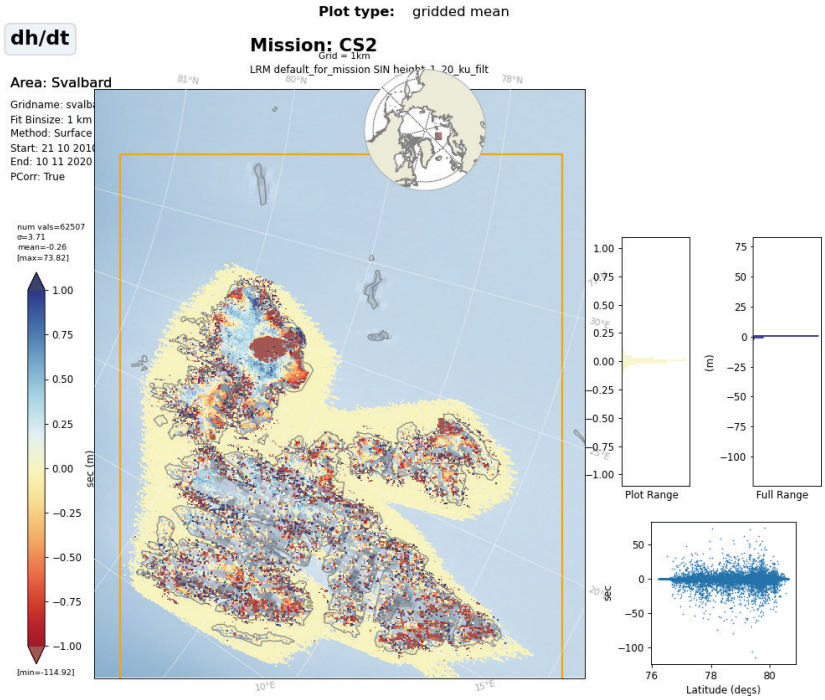


*Figure 3.2: Example figure from metadata, in this case for CS2 Svalbard surface elevation change rates.*

***Data***

The data for a given mission and region is held in one netCDF4 file.

Each grid cell in the region is treated separately. A surface model is fitted to the time-series of measurements in the cell, and is used to derive an estimate of elevation change rate, and surface slope. It is also used to prepare a time-series of surface elevation change in each cell, averaged over the cell area in 30-day epochs. Some details of settings used during model calculation are given in [RD4]. The variables are listed in Table 3.4 and the global attributes contained in Table 3.5.

*Table 3.4: The data file format of the elevation change from altimetry product (variables).*

| Variable | Units | Description |
|---|---|---|
| dhdt_array | m/yr | Surface elevation change rates from surface fit model |
| aX_array, where X is 0 to 7 | n/a | Coefficients of surface fit model, see [RD3] for equation |
| slope_array | degrees | Slopes derived from surface fit model |
| sigma_array | m/yr | Standard deviation of elevation changes from surface fit model |
| rms_array | m/yr | RMS of elevation changes from surface fit model |
| dh_ave | m | Epoch averaged surface elevation changes from surface fit model |
| input_dh_dens | n/a | Number of data points for dh_ave |
| input_dh_stddev | m | Standard deviation of dh data points for dh_ave |
| input_dh_start_time | years since 1991.0 | Time of earliest dh datapoint that went into dh_ave |
| input_dh_end_time | years since 1991.0 | Time of latest dh datapoint that went into dh_ave |
| epoch_lo | years since 1991.0 | Start time of epoch |
| epoch_hi | years since 1991.0 | End time of epoch |
| epoch_lo_dt | years since 1991.0 | Start time of epoch as a string |
| epoch_hi_dt | years since 1991.0 | End time of epoch as a string |

*Table 3.5: The file format of the elevation change from altimetry product (global attributes).*

| Global attributes | Units | Description |
|---|---|---|
| projection | n/a | Map projection of grid, from EPSG |
| grid_x_axis_length_in_m | m | Length of grid along x axis |
| grid_y_axis_length_in_m | m | Length of grid along y axis |
| grid_lower_left_x_in_m | m | X co-ordinate of extreme lower left corner of grid |
| grid_lower_left_y_in_m | m | Y co-ordinate of extreme lower left corner of grid |
| grid_cell_width_in_m | m | Grid cell width |
| first_data_cycle | n/a | Number of first cycle of data used in dataset |
| last_data_cycle | n/a | Number of last cycle of data used in dataset |
| surface_fit_sigma_filter | n/a | Surface fit model is iterated until all datapoints are within this number of standard deviations of the mean. |
| max_surface_fit_iterations _allowed | n/a | Maximum number of iterations of surface fit model allowed |
| max_linear_fit_iterations _allowed | n/a | Maximum number of iterations of linear fit model allowed when deriving dh/dt |

| | | |
|---|---|---|
| min_measurements_in_cell_for_surface_fit | n/a | Minimum number of datapoints required in a cell to allow surface modelling |
| power_correction_applied | True or False | If true, a correction for change in backscatter power as measured during the mission is applied after surface modelling |
| power_correction_length_in_years | yr | If power correction is used, length of period over which power change rate is calculated |
| power_correction_start_date | String formatted as dd mm yyyy | If power correction is used, start of period over which power change rate is calculated |
| power_correction_end_date | String formatted as dd mm yyyy | If power correction is used, end of period over which power change rate is calculated |
| glacial_isostatic_adjustment_model | n/a | Model used to correct dh timeseries for glacial isostatic movements. In this product always ICE-5G, see Peltier, 2004. |
| epoch_length_in_days | days | Averaging period in dh timeseries |
| number_of_epochs | n/a | Number of averaging periods in dh timeseries |

## 3.3 Known limitations

### 3.3.1 Elevation change profiles in HMA from ICESat-2 data

At the moment, the time span for which ICESat-2 data is available (since autumn 2018) is still rather short for analyses based on ICESat-2 data alone, even for polar areas with exact repeats. Double differencing trend analyses with regard to a reference DEM, as described for ICESat laser altimetry data (temporal coverage: 2003-2009) in the previous PUG [RD-1], requires slightly longer data time series to reliably represent multi-year changes. ICESat-2 altimetry changes for the mid-latitudes will thus only become available, and useful, a few years from now.

ICESat-2 altimetry data has a high temporal repeat frequency relative to the DEM availability in the Chongtar region. Although the limited spatial coverage of only six tracks per overpass hampers spatially extensive analyses, ICESat-2 can provide additional temporal information on glacier surface changes in particular for areas with rapid changes, such as the surges of Chongtar glacier. The ATL03 data provides a very good vertical accuracy and along-profile resolution that reveals details of the surface topography (e.g. crevasses) of the glaciers.

### 3.3.2 Surface modelling and time-series over the Eastern Arctic

The surface modelling analysis method assumes a number of conditions that may not be true to a greater or lesser extent:

1. It assumes that a quadratic surface is a good fit to the ground in each cell. This may be true over a large, low-lying glacier, but not necessarily so in rougher terrain.
2. It assumes that a long-enough time-range is present in the data to model long-term trends. The method cannot be applied if a seasonal signal is not properly established. In practice, at least a 2-year long dataset is recommended.
3. It models the long-term elevation trend as constant and uni-directional.
4. It can only be applied to cells where enough good measurements exist to provide a reasonable model fit. In practice, there should be at least 20 data points in each cell, and these should span at least 70% of the time period used in the modelling.

In this case, the product always meets the requirements stated in points 2 and 4.

Note that Sentinel-3B data is only available for a 2-year period, which is only just adequate to establish a seasonal signal, as stated in point 2.

Uncertainties in the dataset are highly mission-dependent, with earlier missions having higher uncertainty levels than later ones. Uncertainties are also highly related to the underlying terrain. A summary of these dependencies is given in [RD5] Section 2.2.1, showing that over low-slope terrain all missions except the earliest (ERS1 and ERS2) have measured accuracy and precision within the GCOS target of 1 m for elevation, as given in [RD6] requirement URq_02.

## 3.4 Software tools and data access

### 3.4.1 Elevation change profiles in HMA from ICESat-2 data

The data are provided in the csv file format. This data format can be imported easily by any programming language and GIS/remote sensing software tools, although performance may be slow for GIS tools visualising the large number of points. The metadata file describes the meaning of each parameter (column) and provides projection information.

### 3.4.2 Surface modelling and time-series over the Eastern Arctic

The data files are in netCDF format, a machine-independent format supported by the Unidata Program Center, and described here; https://doi.org/10.5065/D6H70CW6

A list of software packages, both commercial, and free and open-source, for manipulating and displaying netCDF files, is maintained at;
https://www.unidata.ucar.edu/software/netcdf/software.html

The initial datasets input to the analysis are freely available from;
ERS 1 & 2: https://earth.esa.int/eogateway/catalog/ers-1-2-radar-altimeter-reaper-geophysical-data-record-gdr-ers_alt_2-?text=reaper
EnviSat: https://earth.esa.int/eogateway/catalog/envisat-ra-2-geophysical-data-record-gdr-ra2_gdr__2p-?text=envisat+gdrv3
CryoSat-2: https://earth.esa.int/eogateway/missions/cryosat/data
Sentinel-3 A & B: https://sentinels.copernicus.eu/web/sentinel/sentinel-data-access

For alternative sources of comparable data, see [RD2] Sections 3.3.1 and 3.3.2.

# 4. Elevation change (DEM differencing)

## 4.1 Product content

Changes of glacier geometry or volume can be quantified by analysing DEMs acquired at two points in time. The glacier surface elevation at an individual point changes as a result of glacier accumulation and ablation, which are influenced by meteorological processes, as well as glacier flow with ice emergence or submergence. To provide reliable results, the accuracy and precision of the DEMs has to exceed the expected surface elevation changes. The volume change or geodetic method is used to determine glacier mass balance, in particular for longer-term mass balance trends over the course of several years or even decades. In regions with surging glaciers that undergo rapid geometrical changes, also shorter time intervals may provide interesting insights into the evolution and dynamics of a surge.

The accuracy of DEM differencing depends on the quality of the input DEMs and various required pre-processing and post-processing steps. DEMs can be created using different principles; the most common sources are stereo-photogrammetry from optical imagery and microwave interferometry. Publicly available DEM datasets commonly have a different vertical and horizontal accuracy. To be able to differentiate two DEMs, they need to be re-projected and resampled such that the spatial extent and cell sizes of the two matrices match. Finally, the difference DEM needs to be post-processed to identify and remove outliers, and to assess the quality and uncertainty of the product.

### 4.1.1 DEM differencing in HMA

The DEM differencing product is based on two DEMs with known acquisition dates: The SRTM1 DEM at 1 arcsec (~30 m) resolution from February 2000 (USGS, 2017) and the HMA-DEM mosaic (Shean, 2017) at 8 m spatial resolution. The HMA-DEM is composed of various DEM datasets mostly acquired during 2015 (nine scenes from Feb.-Oct.) in this region, complemented with scenes from 2009-2011 in the very East of the South/North Chongtar glacier accumulation areas (4 scenes), and one scene from 2009 covering parts of the South Chongtar/Sarpo Laggo glacier tongues. The DEMs were projected to UTM 43N (EPSG 32643), elevations were vertically transformed to the WGS 84 ellipsoid and the SRTM DEM was co-registered to the HMA DEM using OPALS (Pfeifer et al., 2014). Specifically, we applied least squares matching to estimate the full 3D affine transformation parameters that minimize the errors with respect to the reference DEM over common stable areas. These were manually digitized off-glacier excluding slope values larger than 40 degrees. Both DEMs were resampled, clipped and aligned to the same 30 m grid. The output differences raster dataset is obtained by subtracting the SRTM DEM from the HMA-DEM (Fig. 4.1). The dataset was filtered for outliers, and co-registration accuracy of the DEMs was computed from elevation differences calculated over stable terrain (off glacier) with slopes smaller than 40°.

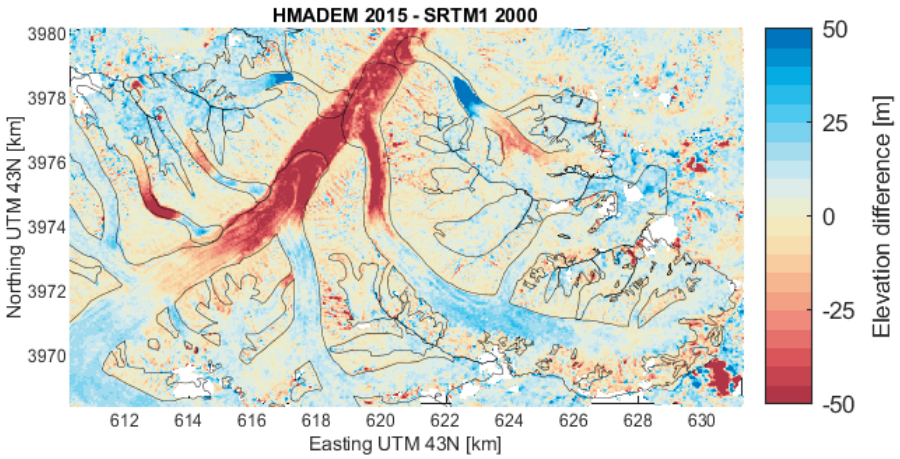


*Figure 4.1: Elevation differences the HMA DEM from 2015 and the SRTM DEM from 2000.*

## 4.2 Product format

### 4.2.1 DEM differencing in HMA

The dataset provides the surface elevation differences of the South Chongtar Glacier, NN9/NN08/NN07 Glacier, North Chongtar Glacier, and Sarppo Lago, located in the central Karakoram at approximately 35.94° N and 76.33° E. The dataset is in geotiff format. Elevation differences are in metres, the pixel spacing is 30 m and the projection is WGS 84 / UTM zone 43N.

## 4.3 Known limitations

Most publicly available DEMs have known inherent limitations that are a direct result from how these DEMs are generated.
General limitations include:

- Data voids that result in limited glacier coverage, or
- locally an unnaturally bumpy glacier surface that results in large elevation errors. For optical stereo DEMs (such as the HMA DEM), voids/elevation errors can be caused by cloud coverage or lack of contrast mainly in the bright, snow-covered glacier accumulation areas. The side-looking geometry of SAR microwave sensors (such as the SRTM DEM) make this data susceptible to layover/foreshortening in steep terrain, where parts of the landscape are not visible to the sensor, resulting in data gaps. In addition, SAR interferometry is susceptible to data gaps in areas with poor phase coherence.
- Microwave penetration into snow and ice can be in the order of decimetres to metres, resulting in surface elevations that are lower than the actual snow/ice surface for SAR-based DEMs such as the SRTM DEM. Microwave penetration depths depend greatly on local snow/ice conditions at the time of acquisition and may vary greatly within space and time. They are thus not straightforward to correct for.
- Elevation errors from mosaicking for products generated from multiple scenes/tiles, such as the HMA DEM.

Elevation errors from these sources may cause local elevation biases of up to several metres.

### 4.3.1 DEM differencing in HMA

The SRTM DEM is based on C-band microwave data, which penetrates into dry snow and ice, and the actual glacier surface may thus have been higher than recorded by the SRTM. We did not correct the SRTM DEM for microwave penetration into ice and snow (Gardelle et al., 2012), as the effect is small compared to the elevation differences caused by the surges and uncertain, i.e. it is not systematic and any – for example elevation dependent correction – can not be justified either. The HMA-DEM is a merged dataset from elevation values from numerous scenes, with the majority of the contributing data dating from early 2015. However, in the very East of the South/North Chongtar glacier accumulation areas and parts of the South Chongtar/Sarpo Laggo glacier tongues, a few scenes from 2009-2011 were used, increasing elevation uncertainty in these areas. Also these uncertainties are small compared to the magnitude of elevation changes caused by the glacier surges (Figure 4.1).

## 4.4 Software tools and data access

### 4.4.1 DEM differencing in HMA

Geotiff datasets can be read by all common geospatial software/GIS, computational software or programming languages (e.g., Matlab, python, R).

# 5. Velocity

## 5.1 Product content

Velocity fields are estimated using optical or microwave repeat satellite data. Block and feature matching techniques (e.g. the normalized cross-correlation) are employed with both data sources. SAR interferometry is used to complement results from microwave data for mapping the flow fields of slow-moving glaciers and to identify the drainage divides of ice caps.

The velocity product from optical images is based upon pre-orthorectified optical images that cover the same glacier(s) within a period of some days to several years. Image matching within an offset tracking procedure is then performed over the intersection of both optical image scenes, both on and off glacier. Off glacier offsets are used for co-registration and adjustment of the displacement field, or internal validation of the product. The output product is the raw co-registered displacements (unfiltered) for the area of interest (scene coverage).

The glacier velocity product from SAR data is commonly based upon images that cover the same glacier(s) within a period of some days to several weeks. Image matching within an offset tracking procedure is performed over the intersection of both SAR image scenes, both on and off glacier, in the original radar geometry. Off-glacier offsets are used for co-registration and internal validation of the product. The native output products of SAR offset-tracking procedures are co-registered displacements in the satellite line-of-sight and along track components for the entire area of interest (scene coverage). For final delivery and comparison with other products (e.g. from optical sensors), the raw satellite line-of-sight displacements are transformed to 3D velocity maps by assuming that flow occurs parallel to the ice surface as estimated from a DEM and orthorectified to a specific geographic projection.

SAR interferometry for ice velocity mapping over glaciers exploits SLC data with short repeat-pass periods (typically a few days) in order to preserve coherence. SAR interferometry processing follows classical procedure including image coregistration, phase calculation, phase filtering, phase unwrapping, phase calibration and geocoding [RD4]. The basic output products of SAR interferometry are line-of-sight (LOS) velocity maps of regions preserving phase coherence. The individual LOS velocity maps lead to an ambiguity of the ice velocity vector and results from different dates and tracks are therefore combined together to generate a 2D horizontal velocity map. The 2D velocity field is obtained through a pixel-by-pixel least-square inversion from the LOS geometry to the geocoded one.

### 5.1.1 Ice surface velocity in the HMA from optical data

In this study, we calculated the glacier flow velocities of the surges of three glaciers located in the central Karakoram at approximately 35.94° N and 76.33° E: North and South Chongtar Glacier and an unnamed glacier referred to as NN9. We provide the 2D surface flow velocities map derived from available optical (Sentinel-2, Landsat and Planet) before and during the glacier surge (Fig. 5.1). The normalized cross-correlation algorithm implemented in the correlation image analysis software (CIAS, Kääb and Vollmer, 2000) is used to calculate the glacier surface displacement between optical satellite image pairs.

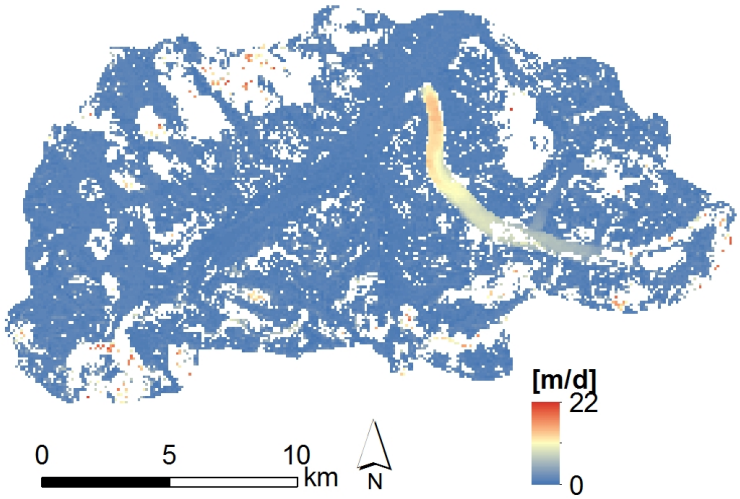


*Figure 5.1: 2D surface flow velocities of South Chongtar derived from Sentinel-2 between November 3 and 8, 2020.*

### 5.1.2 Ice surface velocity in HMA from TerraSAR-X offset-tracking

This data set provides detailed ice velocity maps of glaciers in the Karakoram region, including Chongtar Glacier (Fig. 5.2). The ice velocity is derived by applying SAR offset tracking using high-resolution repeat-pass SAR data of the TanDEM-X (TDM) satellite constellation, consisting of the twin satellites TerraSAR-X (TSX) and TanDEM-X (TDX). We used single look slant range complex (SSC) images acquired in Stripmap Mode (SM), with a cross- and along-track resolution reaching up to 3 m. We selected three image pairs from two different tracks covering the region around Chongtar Glacier in descending direction and acquired in 2011, 2012 and 2014. The repeat-pass period of the selected scenes ranges between 22 and 77 days and cover the periods: 2011/11/12-2011/12/04, 2012/09/09- 2012/11/25 and 2014/04/10-2014/05/24. For the offset tracking, a template size of 96×96 pixels was used for generating velocity maps with a 50 m grid spacing, geocoded using the 90 m SRTM v4 DEM (Jarvis et al., 2008) that was resampled to 50 m in UTM 43N projection. As a post-processing step a 9x9 inverse-distance median filter was applied to remove outliers and fill in small gaps.

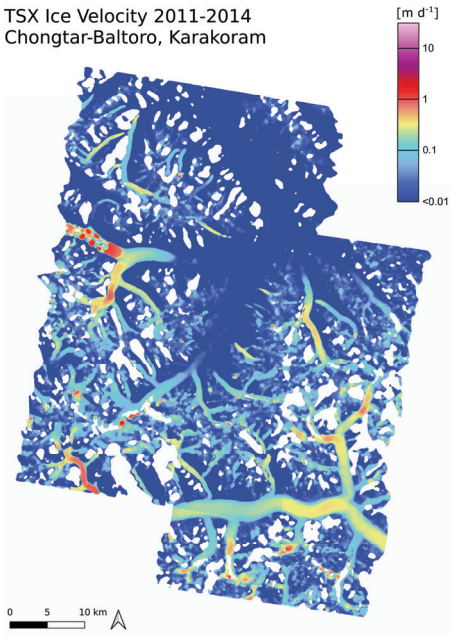


*Figure 5.2: Ice velocity map of the Chongtar-Baltoro region in the Karakoram based on TerraSAR-X.*

### 5.1.3 Ice surface velocity in the Eastern Arctic from offset-tracking of past spaceborne satellite SAR data

Nearly complete mosaics of winter ice surface velocities for the 1990's over the Eastern Arctic (Novaya Zemlya, Franz-Josef-Land, Severnaya Zemlya and Svalbard) were compiled based on historical SAR data. Offset-tracking to JERS-1 SAR data of the time period 1992-1998 was mainly applied. Data gaps were complemented using ERS-1 SAR data of the time period 1991-1992 (Section 5.1.3). In addition, velocity maps computed with offset-tracking of 2008-2011 ALOS-1 PALSAR-1 data are provided. The offset-tracking algorithm of the Gamma software (Strozzi et al., 2002; Werner et al., 2005) was considered for data analysis.

### 5.1.4 Ice surface velocity in Svalbard from ERS-1/2 InSAR

Data gaps in the mosaic of winter ice surface velocities for the 1990's over Svalbard from offset-tracking of past spaceborne satellite SAR data were complemented using SAR interferometry of ERS-1/2 SAR data of the time period 1995-1997 (Fig. 5.3). A ERS-1/2 InSAR ice velocity map of Nordaustlandet (Svalbard) combines interferometric phases from 1-day ERS-1/2 image pairs and is produced for the winter 1995/1996 at 100 m resolution (Dowdeswell et al., 2008). An ERS-1/2 InSAR ice velocity map of south Spitsbergen is produced from winter 1996 and 1997 data at 20 m resolution (Nuth et al., 2019).

### 5.1.5 Ice surface velocity in the Eastern Arctic from offset-tracking of Sentinel-1 SAR data

The offset-tracking algorithm of the Gamma software (Strozzi et al., 2002; Werner et al., 2005) was used to compute ice surface velocities over the Eastern Arctic (Novaya Zemlya, Franz-Josef-Land, Severnaya Zemlya and Svalbard) from Interferometric Wide Swath Sentinel-1 SAR data available from Copernicus as SLC data. All available image pairs with 12-day time interval were considered. These data are available on *request* from the *authors*. Sentinel-1 mosaics computed from winter 2020/2021 data (Fig. 5.4) can be downloaded from cryoportal.enveo.at.

### 5.1.6 Ice surface velocity in Svalbard from Sentinel-1 interferometry

The first Sentinel-1 ice velocity (IV) product over Svalbard is derived by applying the SAR interferometry (InSAR) technique. The Svalbard InSAR IV is an average solution of the individual InSAR results calculated for Sentinel-1 6-day pairs acquired in Interferometric Wide (IW) swath mode during the winter period from October 2018 to March 2019, combining crossing ascending and descending orbits in a least-square sense. Due to the lack of crossing orbits over the Nordauslandet ice cap, the coverage of the InSAR IV map there is only partial. The InSAR IV map is provided at 50 m grid spacing and the snow-free regions of the archipelago are not masked (Fig. 5.5 (a)). The Svalbard InSAR map of the individual velocity components is provided along with the velocity magnitude, the error standard deviation on the individual velocity components and the count of valid observations used for each pixel of the composite map. A masking of areas with low coherence is applied during the interferometric processing, thus leading to a variable spatial coverage of one pair to the other and a non-comprehensive coverage of the final map. The number of valid observations used to derive the velocity field may therefore vary locally. Sentinel-1 pairs included in the final map are selected by visual inspection, those showing large errors in the InSAR results being dismissed from the dataset. The selected dataset results from a trade-off between keeping a satisfactory coverage and minimizing errors.

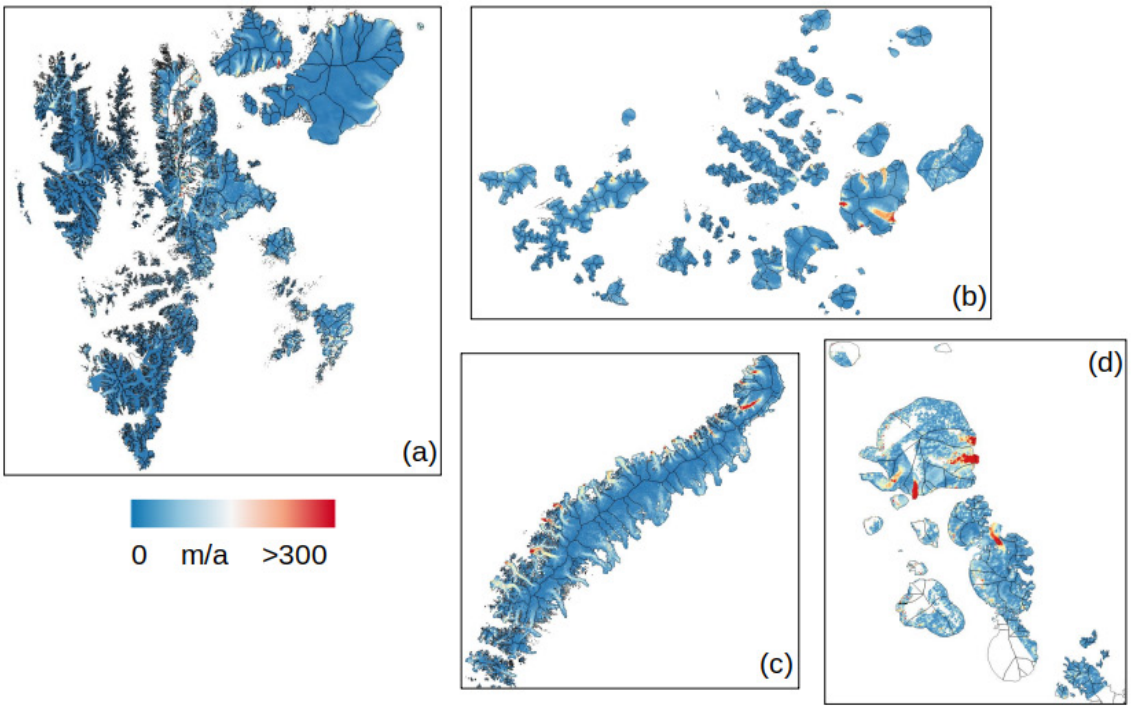


*Figure 5.3: Ice velocity maps for: (a) Svalbard from ERS-1/2 InSAR (1995.12.10-1995.01.29), JERS-1 (1994.02.05-1998.03.26) and (ERS-1 1992.01.03-1992.01.15); (b) Franz-Josef-Land from JERS-1 (1996.04.04-1998.05.29) and ERS-1 (1991.10.12-1991.11.17); (c) Novaya Zemlya from JERS-1 (1998.01.21-1998.03.25); (d) Severnaya Zemlya from ERS-1 (1991.10.18-1992.03.02).*

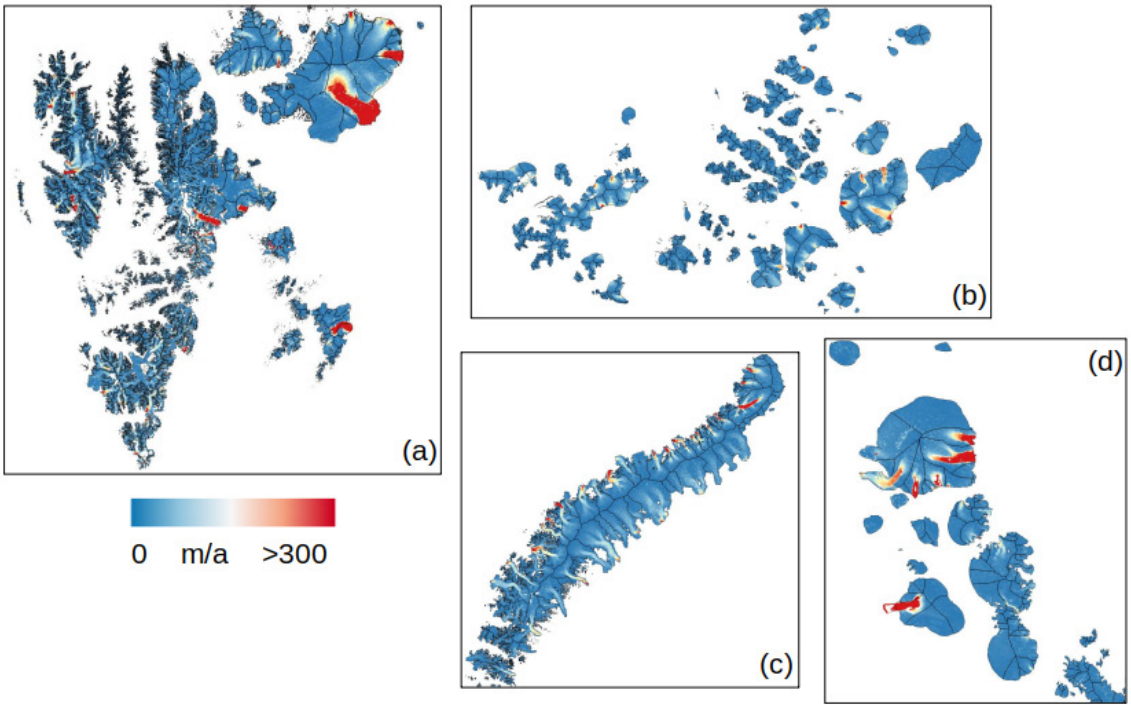


*Figure 5.4: Ice velocity maps from Sentinel-1 for: (a) Svalbard (2021.01.26-2021.02.12); (b) Franz-Josef-Land (2021.01.10-2021.02.12); (c) Novaya Zemlya (2021.02.04-2021.02.25); (d) Severnaya Zemlya (2020.12.15-2021.02.25).*

### 5.1.7 Ice surface velocity in Svalbard from Sentinel-1 interferometry and offset-tracking flow direction

The second Sentinel-1 ice velocity (IV) product over Svalbard is derived by applying the SAR interferometry (InSAR) technique combined with the flow direction obtained from an offset-tracking (OT) map. The offset-tracking map from which the flow direction is derived is based on all Sentinel-1 6- and 12-day pairs acquired in IW mode before 03/05/2018. Knowing the flow direction and assuming it is stable, the velocity magnitude can be derived from InSAR with a single track, thus enhancing the spatial coverage of the IV map compared to the InSAR map using only crossing orbits. In this case, the velocity cannot be estimated in regions with zero velocity (no flow), e.g. close to the ice divides. The IV map is an average solution of the InSAR results calculated for Sentinel-1 6-day pairs acquired in IW mode during the winter period from October 2018 to March 2019. It is provided at 50 m grid spacing. The ice-free regions of the archipelago are not masked (Fig. 5.5 (b)). The dataset is used to generate the final map as in the case of the InSAR IV map. The Svalbard IV map combining InSAR and OT flow direction is provided along with the velocity magnitude, the error standard deviation on the velocity magnitude and the count of valid observations used for each pixel of the map. Where valid number of observations is equal to 1, the standard deviation cannot be estimated.

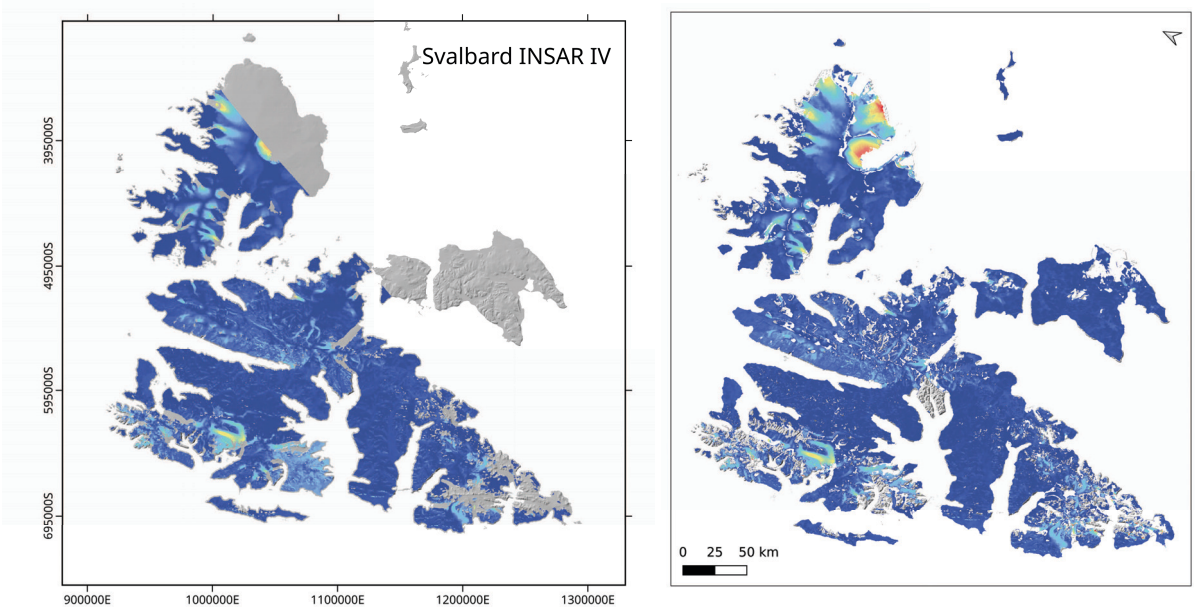


*Figure 5.5: Svalbard ice velocity magnitude: (a) Sentinel-1 SAR interferometry from crossing ascending and descending orbits (01/10/2018 – 01/03/2019); (b) combination of Sentinel-1 SAR interferometry and the flow direction from the offset-tracking IV map (01/10/2018 – 01/03/2019).*

## 5.2 Product format

### 5.2.1 Ice surface velocity in the HMA from optical data

The surface velocity of South Chongtar Glacier, NN9 Glacier, and North Chongtar before surging is derived using Sentinel-2 (Band 8) image pairs, acquired between 2016 and 2020, and Landsat7 and Landsat 8 (Band 8) image pairs, acquired between 2000 and 2002 and 2013 and 2019. In order to analyse the surging phase of the South Chongtar glacier, ice velocity is derived using Sentinel-2 (Band 8) image pairs, acquired between Sep 2019 and May 2021 as

well as Planet (NIR band) image pairs, acquired between June 2020 and October 2020. The size of the search area for the image correlation is set in relation to the maximum displacement estimated between two satellite scenes and it varies for almost each images pair. This information is not reported in the metadata. The length of the displacements is converted to physical units (metres/day, m/d) using the temporal difference between the satellite image pairs. Outliers are removed in post-processing and data voids are not interpolated. The ice velocity map (m/d) is provided in geotif format and the acquisition dates are provided in the file name. The pixel spacing is 100 m and the projection is WGS 84 / UTM zone 43N.

### 5.2.2 Ice surface velocity in HMA from TerraSAR-X offset tracking

The dataset is provided in a zipped file containing the ice velocity maps in GeoTIFF format. The pixel spacing is 50 m and the projection is WGS 84 / UTM zone 43N (EPSG: 32643). Velocity is provided in meters per day in three-layer geotiffs representing the ice velocity components $v_x$, $v_y$, $v_z$. Also provided are geotiffs with the horizontal magnitude and a quicklook image. The size of the compressed file is 21 MB.

### 5.2.3 Ice surface velocity in the Eastern Arctic from offset-pracking of past spaceborne satellite SAR data

Two sets of data containing historical ice surface velocities over the Eastern Arctic (Novaya Zemlya, Franz-Josef-Land, Severnaya Zemlya and Svalbard) are provided.

The velocities derived from offset-tracking of ERS-1 (1991-1992), JERS-1 (1992-1998) and ALOS-1 PALSAR-1 (2006-2011) data are available in vector format with metadata information for single image tracks, see description in [RD1]. A comma-separated values (csv) file provides the northing and easting coordinates of measurement points, the elevation, the displacement in metres in the x, y and z directions, and the cross-correlation coefficient for each measurement. A metadata file in xml format provides information about the SAR images used, the processing parameters and quality aspects of the data such as the percent of valid information over ice and statistical measures over ice-free regions. In addition, for each image pair geotiff's of the three-dimensional ice surface displacement maps, the two intensity images, the differential interferogram, the phase coherence image, an RGB color composite of the coherence, intensity and intensity difference between both images, and the layover and shadow map are available. In all cases data are provided in UTM projection (zones 33N for Svalbard, 40N for Novaya Zemlya and Franz-Josef Land, and 47N for Severnaya Zemlya) with a spatial resolution of 100 m.

The second set of data contains velocity mosaics of the best JERS-1 results over Novaya Zemlya, Franz-Josef-Land, and Svalbard, the best ERS-1 results over Franz-Josef-Land, Severnaya Zemlya and Svalbard and the best ALOS-1 PALSAR-1 results over Novaya Zemlya, Franz-Josef-Land, and Svalbard in geotif format.

### 5.2.4 Ice surface velocity in Svalbard from ERS-1/2 InSAR

The ERS-1/2 InSAR three-dimensional ice surface displacement maps of Nordaustlandet (Svalbard), South Svalbard and North-West Svalbard are available in geotif format.

### 5.2.5 Ice surface velocity in the Eastern Arctic from offset-tracking of Sentinel-1 SAR data

The ice surface velocities over the Eastern Arctic (Novaya Zemlya, Franz-Josef-Land, Severnaya Zemlya and Svalbard) are provided in vector format with metadata information for single image tracks, see description in [RD1] and Section 5.2.1. In addition, velocity mosaics of the best Sentinel-1 results over Svalbard, Franz-Josef-Land, Novaya Zemlya and Svalbard, for the winter 2020/2021 are available in geotif format.

### 5.2.6 Ice surface velocity in Svalbard from Sentinel-1 interferometry and interferometry combined with offset-tracking flow direction

The maps are provided in zipped files including raster files of 2-D velocity field components ($v_x$, $v_y$), the velocity magnitude, the standard deviation on the $v_x$ and $v_y$ components and the count of valid observations. The files are listed in Table 5.1 and Table 5.2. All raster files are distributed in geotif format with polar stereographic projection (EPSG:3413) and 50 m grid spacing. The 2-D velocity field consists of a raster corresponding to $v_x$ (Easting component) and a second raster corresponding to $v_y$ (Northing component). The x- and y-component refer to the axis directions of the projection reference system and the velocity values are provided in meters per day. In addition to the raster files, a README and a DESCRIPTION text file that briefly describe the dataset content, naming and format are included in the compressed dataset.

*Table 5.1: Description of InSAR IV dataset content.*

| Raster name | Description |
|---|---|
| Svalbard_iv_50m_s1_epsg3413_insar_s20181001_e201903 | IV Easting component [m/day] |
| Svalbard_iv_50m_s1_epsg3413_insar_s20181001_e201903 | IV Northing component [m/day] |
| Svalbard_iv_50m_s1_epsg3413_insar_s20181001_e201903 | Ice velocity magnitude [m/day] |
| Svalbard_iv_50m_s1_epsg3413_insar_s20181001_e201903 | Standard deviation of the IV East |
| Svalbard_iv_50m_s1_epsg3413_insar_s20181001_e201903 | Standard deviation of the IV |
| Svalbard_iv_50m_s1_epsg3413_insar_s20181001_e201903 | Valid observation count [#] |

*Table 5.2: Description of InSAR and OT flow direction IV dataset content.*

| Raster name | Description |
|---|---|
| Svalbard_iv_50m_s1_epsg3413_insar_s20181001_e20190301 | IV Easting component [m/day] |
| Svalbard_iv_50m_s1_epsg3413_insar_s20181001_e20190301 | IV Northing component [m/day] |
| Svalbard_iv_50m_s1_epsg3413_insar_s20181001_e20190301 | Ice velocity magnitude [m/day] |
| Svalbard_iv_50m_s1_epsg3413_insar_s20181001_e20190301 | Standard deviation of the IV |
| Svalbard_iv_50m_s1_epsg3413_insar_s20181001_e20190301 | Valid observation count [#] |

## 5.3 Known limitations

### 5.3.1 Ice surface velocity in the HMA from optical data

The uncertainties of glacier flow velocity estimations from optical satellite images are mainly related to co-registration accuracy, orthorectification, the time interval between image pairs as well as surface conditions (shadow, snow) and the pixel size of the satellite images. Clouds

and snow cover have been identified as a major challenge. In the HMA study, the selection of the satellite pair prioritized the reduction of cloud cover on South Chongtar rather than NN9 and North Chongtar, which were rarely cloud-free. Hence, it is not only spatial resolution that is responsible for data limitations. The velocity uncertainty results of optical sensors suggest that the larger is the time window between two pairs (which is associated with a pre-surging phase) and hence slower velocity, the smaller the uncertainty on the measured displacement. However, despite the short interval, the uncertainty is higher for Planet than for Sentinel-2. For Sentinel-2, the orthorectification error is minimized because the imagery comes from the same relative orbit. On the contrary, we have different orbital paths between Planet image pairs. All three optical sensors can be used to derive the temporal evolution of flow velocities - cloud cover, snow conditions and cast shadow permitting. The main point to consider is an adjustment of the temporal spacing between image pairs with the flow velocities.

### 5.3.2 Ice surface velocity in the Eastern Arctic from satellite SAR data

Uncertainties in winter ice surface velocity estimations originate from errors in tracking offsets between image pairs, see description in [RD1], as well as unknown representativeness of winter velocity mosaics with regard to the annual average velocities. In order to infer in how far the mosaics computed from SAR data over short time-intervals (typically 1 to 44 days) for several winter seasons in the 1990's are representative of annual average results, short-term variability in glacier flow from Sentinel-1 data regularly available since 2015 with 12-day repetition rate are analysed in Strozzi et al. (in rev.). In most of the cases it was found that winter velocities are a good representative of mean annual velocities and give a good idea of long-term trends in speed. Seasonal fluctuations in winter are relatively small for non-surging glaciers, with an underestimation of less than 10%, in particular over the Russian High Arctic. Summer velocities, on the other hand, can be significantly larger than the annual mean. Additionally, there are strong, short-time speed-up events during the summer period for many glaciers.

### 5.3.3 Ice surface velocity from Sentinel-1 and TerraSAR-X

The InSAR and offset tracking IV products have some limitations. Here is a summary of the main ones:

- They contain separate layers for the horizontal (Easting, Northing) and the vertical components of velocity. This is, however, not the true 3D velocity, which requires both ascending and descending image pairs acquired close in time.
- The IV products do not have a time stamp for a single date but give the average velocity over the time-period covered.

In regions of complex topography such as the Svalbard archipelago or in areas of fast flow and shearing, interferometry performs poorly. Coherence masking is applied during the processing, leaving some gaps. Some regions are prompt to phase unwrapping errors and some erroneous estimates are left in the final product.

The limitations of the IV dataset combining InSAR and OT flow direction include those listed for the InSAR map. In addition to these limitations, this technique is not able to retrieve the velocity estimates in regions with ice flow speed close to zero, e.g. close to ice divides, as the uncertainty on the flow direction becomes very large in such areas.

## 5.4 Software tools and data access

Datasets in geotif format can be readily ingested and displayed by any GIS package (e.g. the popular open-source GIS package QGIS). Most software packages are also capable to import text-delimited files such as csv. Further, the csv can be converted to a shapefile for viewing the dataset in geospatial software (e.g. ArcGIS, GRASS, QGIS).

Nearly all datasets can be downloaded through the ESA Glacier CCI+ database (http://glaciers-cci.enveo.at). The Sentinel-1 surface velocities with 12-day time interval over the Eastern Arctic are available on request from the authors. However, Sentinel-1 mosaics computed from winter 2020/2021 data can be downloaded from cryoportal.enveo.at. The ice surface velocity data set for the 1990's over the Eastern Arctic from satellite SAR data can also be downloaded from https://doi.pangaea.de/10.1594/PANGAEA.938381 (Strozzi et al., in rev.).

# 6. References

Berthier, E. and Brun, F.: Karakoram geodetic glacier mass balances between 2008 and 2016: persistence of the anomaly and influence of a large rock avalanche on Siachen Glacier, J. Glaciol., 65, 494–507, 2, 2019.

Brenner, A., DiMarzio, J. and Zwally, H.: Precision and Accuracy of Satellite Radar and Laser Altimeter Data Over the Continental Ice Sheets, IEEE T. Geosci. Remote, 45, 321–331, 2007.

Dowdeswell J., T. Benham, T Strozzi and J.O. Hagen: Iceberg calving flux and mass balance of the Austfonna ice cap on Nordaustlandet, Svalbard, Journal of Geophysical Research, 133, F03022, doi:10.1029/200tJF000905, 2008.

Gardelle, J., Berthier, E., Arnaud, Y., and Kääb, A.: Region-wide glacier mass balances over the Pamir-Karakoram-Himalaya during 1999–2011, The Cryosphere, 7, 1263–1286, 2013.

Hugonnet, R., McNabb, R., Berthier, E., Menounos, B., Nuth, C., Girod, L., Farinotti, D., Huss, M., Dussaillant, I., Brun, F., and Kääb, A.: Accelerated global glacier mass loss in the early twenty-first century, Nature, 592, 726–731, 2021.

Leclercq, P. W., Kääb, A., and Altena, B.: Brief communication: Detection of glacier surge activity using cloud computing of Sentinel-1 radar data, The Cryosphere, 15, 4901–4907, 2021.

Leinss, S. and P. Bernard TanDEM-X: Deriving InSAR Height Changes and Velocity Dynamics of Great Aletsch Glacier, IEEE Journal of Selected Topics of Applied Earth Observation and Remote Sensing, accepted for publication.

Li, S., S. Leinss and I. Hajnsek, Cross-Correlation Stacking for Robust Offset Tracking using SAR Image Time-Series, IEEE Journal of Selected Topics in Applied Earth Observations and Remote Sensing, PP (99):1-1, doi:10.1109/JSTARS.2021.3072240, 2021.

McMillan, M., Muir, A., Shepherd, A., Escolà, R., Roca, M., Aublanc, J., Thibaut, P., Restano, M., Ambrozio, A., and Benveniste, J. (2019): Sentinel-3 Delay-Doppler altimetry over Antarctica, The Cryosphere, 13, 709–722, 2019.

Neumann, T. A., A. Brenner, D. Hancock, J. Robbins, J. Saba, K. Harbeck, A. Gibbons, J. Lee, S. B. Luthcke, T. Rebold, et al. 2021. ATLAS/ICESat-2 L2A Global Geolocated Pho-ton Data, Version 4. Boulder, Colorado USA. NASA National Snow and Ice Data Center Distributed Active Archive Center. https://doi.org/10.5067/ATLAS/ATL03.004. [Last ac-cessed 16 Octoctober 2021].

Nilsson, J., Gardner, A., Sandberg Sørensen, L., and Forsberg, R.: Improved retrieval of land ice topography from CryoSat-2 data and its impact for volume-change estimation of the Greenland Ice Sheet, The Cryosphere, 10, 2953–2969, 2016.

Nuth, C., Gilbert, A., Köhler, A., McNabb, R., Schellenberger, T., Sevestre, H., Weidle, C., Girod, L., Luckman, A., and Kääb, A.: Dynamic vulnerability revealed in the collapse of an Arctic tidewater glacier, Scientific Reports, 9, 5541, https://doi.org/10.1038/s41598-019-41117-0, 2019.

Paul, F., T. Bolch, A. Kääb, T. Nagler, C. Nuth, K. Scharrer, A. Shepherd, T. Strozzi, F. Ticconi, R. Bhambri, E. Berthier, S. Bevan, N. Gourmelen, T. Heid, S. Jeong, M. Kunz, T.R. Lauknes, A. Luckman, J. Merryman, G. Moholdt, A. Muir, J. Neelmeijer, M. Rankl, J. Van Looy and T. Van Niel, The glaciers climate change initiative: Methods for creating glacier area, elevation change and velocity products, Remote Sensing of Environment, 162: 408–426, 2015.

Paul, F., T. Bolch, K. Briggs, A. Kääb, M. McMillan, R. McNabb, T. Nagler, C. Nuth, P. Rastner, T. Strozzi and J.Wuite, Error sources and guidelines for quality assessment of glacier area, elevation change, and velocity products derived from satellite data in the Glaciers_cci project, Remote Sensing of Environment, 203: 256-275, 2017.

Paul, F., Piermattei, L., Treichler, D., Gilbert, L., Girod, L., Kääb, A., Libert, L., Nagler, T. Strozzi, T. and Wuite, J. (in rev.): Three different glacier surges at a spot: What satellites observe and what not. The Cryosphere Discuss.,

Pfeifer, N., Mandlburger, G., Otepka, J., and Karel, W.: OPALS – A framework for Airborne Laser Scanning data analysis, Computers, Environment and Urban Systems, 45, 125–136, 2014.

Raynal, M. and Jettou, G. (2021): S3MPC STM Annual Performance Report - Year 2020, accessed Nov 2021 (https://sentinels.copernicus.eu/documents/247904/3519647/Sentinel-STM-Annual-Performance-Report-2020.pdf/2887259c-d168-c0ee-0d5a-5fec11926aba?t=1621611181956).

Schröder, L., Horwath, M., Dietrich, R., Helm, V., van den Broeke, M. R., and Ligtenberg, S. R. M. (2019): Four decades of Antarctic surface elevation changes from multi-mission satellite altimetry, The Cryosphere, 13, 427–449, 2019.

Smith, B., Fricker, H. A., Gardner, A., Siegfried, M. R., Adusumilli, S., Csathó, B. M., Holschuh, N., Nilsson, J., Paolo, F.S, and the ICESat-2 Science Team: ATLAS/ICESat-2 L3A Land Ice Height, Version 3, NASA NSIDC Distributed Active Archive Center [dataset], https://doi.org/10.5067/ATLAS/ATL06.003, 2020, [last access: 3 December 2020].

Strozzi, T., A. Luckman, T. Murray, U. Wegmüller, and C. Werner, Glacier motion estimation using SAR offset-tracking procedures, IEEE Transactions on Geoscience and Remote Sensing, 40 (11), 2384-2391, 2002.

Strozzi, T., F. Paul, A. Wiesmann, T. Schellenberger, and A. Kääb, Circum-Arctic Changes in the Flow of Glaciers and Ice Caps from Satellite SAR Data between the 1990s and 2017, Remote Sensing, 9(9), 947, doi:10.3390/rs9090947, 2017.

Strozzi, T., Kouraev, A., Wiesmann, A., Wegmüller, U., Sharov, A., and Werner, C.: Estimation of Arctic glacier motion with satellite L-band SAR data, Remote Sensing of Environment, 112, 636–645, 2008.

Strozzi, T., Paul, F., Wiesmann, A., Schellenberger, T., and Kääb, A.: Circum-Arctic Changes in the Flow of Glaciers and Ice Caps from Satellite SAR Data between the 1990s and 2017, Remote Sensing, 9, 947, 2017.

Strozzi, T., Wiesmann, A., Kääb, A., Schellenberger, T. and Paul, F. (in review): Ice surface velocity in the Eastern Arctic from historical satellite SAR data. Earth System Science Data Discussions, https://doi.org/10.5194/essd-2022-44.

# Acronyms

| | |
|---|---|
| ADP | Algorithm Development Plan |
| ALOS | Advanced Land Observing Satellite |
| ASTER | Advanced Spaceborne Thermal Emission and Reflection Radiometer |
| ATM | Airborne Topographic Mapper |
| CC | Correlation Coefficient |
| CRDP | Climate Research Data Package |
| DEM | Digital Elevation Model |
| DGPS | Differential Global Positioning System |
| ECA | Elevation Change Altimetry |
| ENVISAT | Environmental Satellite |
| EO | Earth Observation |
| ERS | European Remote-Sensing Satellite |
| ETM+ | Enhanced Thematic Mapper plus |
| FAU | Friedrich-Alexander Universität Erlangen-Nürnberg |
| GAMDAM | Glacier Area Mapping for Discharge from the Asian Mountains |
| GLAS | Geoscience Laser Altimeter System |
| GLIMS | Global Land Ice Measurements from Space |
| GO | Glacier Outline |
| GoLIVE | Global Land Ice Velocity Extraction from Landsat 8 |
| GPS | Global Positioning System |
| GRACE | Gravity Recovery and Climate Experiment |
| HMA | High Mountain Asia |
| ICESat | Ice, Cloud, and land Elevation Satellite |
| ID | Identifier |
| InSAR | Interferometric SAR |
| ITS LIVE | Inter-Mission Time Series of Land Ice Velocity and Elevation |
| IV | Ice Velocity |
| IW | Interferometric Wide |
| JERS | Japanese Earth Resources Satellite 1 |
| L8 | Landsat 8 |
| MAD | Median of Absolute Differences |
| MEaSUREs | Making Earth System Data Records for Use in Research Environments |
| NSIDC | National Snow and Ice Data Center |
| OPALS | Orientation and Processing of Airborne Laser Scanning |
| OT | Offset Tracking |
| PALSAR | Phased Array type L-band Synthetic Aperture Radar |
| PVIR | Product Validation and Intercomparison Report |
| PVP | Product Validation Plan |
| QA | Quality Assessment |
| RA | Radar Altimeter |
| RADAR | Radio Detection and Ranging |
| RGI | Randolph Glacier Inventory |
| RLA | Riegl Laser Altimeter |
| RSME | Root Mean Square Error |
| S-1 | Sentinel-1 |

| | |
|---|---|
| S-2 | Sentinel-2 |
| SAR | Synthetic Aperture Radar |
| SARIn | SAR Interferometry mode |
| SIRAL | SAR Interferometer Radar Altimeter |
| SNR | Signal-to-Noise Ratio |
| SPOT | Satellite Pour l'Observation de la Terre |
| SRAL | SAR Altimeter |
| SRTM | Shuttle Radar Topography Mission |
| STD | Standard Deviation |
| TSX | TerraSAR-X |
| UCR | Uncertainty Characterisation Report |
| URD | User Requirements Document |